Detection, classification, and location of seismovolcanic tremors with multi-component seismic data, example from the Piton de la Fournaise volcano (La Réunion, France)

Journeau, C.[1,2], N.M. Shapiro[1,3], L. Seydoux[1], J. Soubestre[3], V. Ferrazzini[5,6] and A. Peltier[5,6]

[1]Institut des Sciences de la Terre, Université Grenoble Alpes, CNRS (UMR5275), Grenoble, France.

[2]Département de Géosciences, Ecole Normale Supérieure, PSL Res. Univ., Paris, France.

[3]Schmidt Institute of Physics of the Earth, Russian Academy of Sciences, Moscow, Russia.

[4]Instituto Volcanológico de Canarias (INVOLCAN), INtech La Laguna, Tenerife, Spain.

[5]Université de Paris, Institut de physique du globe de Paris, CNRS, F-75005 Paris, France.

[6]Observatoire Volcanologique du Piton de la Fournaise, Institut de Physique du Globe de Paris, Université de Paris, CNRS (UMR 7154), La Réunion, Paris, France.

Key Points:

- Use of inter-components cross-correlations methods to analyze volcanic tremors at Piton de la Fournaise volcano
- Detection and classification of the three eruptive tremors occuring in 2010
- Location of tremor and VT sources and highlighting of a pre-eruptive seismic sources migration from the sea level to the eruptive site

Corresponding author: Cyril Journeau, `cyril.journeau@univ-grenoble-alpes.fr`

Abstract

We apply three different methods based on the analysis of the multi-component seismic data to detect and to classify the seismovolcanic tremors and to locate their sources. We use continuous seismograms recorded during one year by 21 stations at the Piton de la Fournaise volcano (La Réunion, France). The first method allows to detect tremors based on stability in time of the inter-components cross-correlations function. Two other methods based on the simultaneous analysis of the whole network can be used to detect tremors and to locate their sources. The second method consists in performing the 2D back-projection of the inter-stations cross-correlations in order to calculate the network response function. In a third approach, the seismic wavefield is analyzed by calculating the width of the network covariance matrix eigenvalue distribution. Simultaneous analysis of the parameters measured by the three different methods can be used to classify different types of tremors. Our results demonstrate that all three methods efficiently detect volcanic tremors accompanying the 2010 eruptions and the preceding pre-eruptive seismic swarms. Furthermore, methods 2 and 3 based on simultaneous analysis of the whole network detect a large number of volcanic earthquakes. Our location results show that each tremor is located in a distinct region of the volcano, close to the eruptive site at a shallow depth and the preceding seismic crisis is located deeper at about the sea level under the summit crater.

1 Introduction

The generation of seismic waves in volcanoes is linked to the movement of magma and related hydrothermal fluids, and to their complex interactions with solid rock (e.g., Roman & Cashman, 2006; McNutt & Roman, 2015). Thus, the interpretation of these signals and the quantification of their source mechanisms allow us to better understand the oscillatory behavior of volcanic systems and the underlying processes. Volcanic activity is generally accompanied by a large spectrum of seismic signals from pre-eruptive seismic swarms to seismic eruptive tremors.

Volcanic tremors (e.g., McNutt & Nishimura, 2008) are part of the long-period (LP) seismicity (B. A. Chouet, 1996). They are ground vibrations with a sustained amplitude lasting from minutes to months, characterized by a low-frequency content (0.5 - 5 Hz). Volcanic tremors accompany eruptions and are often synonymous with the arrival of magma at the subsurface and the first signs of degassing. Therefore, they are a key element in volcano monitoring and a thorough study of these signals could allow us to bring new infor-

mation about volcanic system and to develop new methods of eruption forecasting. They can be caused by several volcanic processes including magma-hydrothermal interactions and magmatic degassing (e.g., B. Chouet & Matoza, 2013) but their physical origin is poorly understood and the study of their source is part of the current challenges of the modern volcanic seismology.

In this study, we focus on the detection, location and characterization of tremors occurring at the Piton de la Fournaise (PdF) volcano. We apply methods based on inter-stations and inter-components cross-correlations. We analyze the data recorded by the PdF seismic network during the 2010 year when three eruptions occurred (see Figure 1 for the positions of eruptive fissures and associated lava flows):

- **the January eruption** that lasted 11 days from 02.01.2010 to 12.01.2010 with the eruptive fissure located on the west part of the summit cone, inside the Dolomieu crater
- **the October eruption** that lasted 17 days from 14.10.2010 to 31.10.2010 with the eruptive site located in the south flank of the volcano
- **the December eruption** that lasted about 15 hours between the 09.12.2010 and the 10.12.2010 with the eruptive site located in the northwestern part of the caldera.

These three eruptions were preceded by pre-eruptive seismic crises and accompanied by seismo-volcanic tremors starting at the onset of the eruption.

Piton de la Fournaise volcano and its seismic network are introduced in part 2. Then, a rapid description of its tremors is made in part 3. The methods applied in this study are described in part 4, with the obtained results presented in part 5 and discussed in part 6.

2 The Piton de la Fournaise volcano and the seismic monitoring system

La Réunion is a volcanic island located in the southwest of the Indian ocean in the Marscarene Basin (Figure 1). Based on dating and geodynamic reconstruction, its volcanism is thought to have a hot spot origin and being generated by the same mantle plume that produced the Deccan Trapp about 65 Ma ago (Courtillot et al., 1986). The head of this mantle plume would have been passed beneath La Réunion about 5 Ma and would be now located 300 km southwest of the island (Bonneville, 1990). Tsekhmistrenko et al. (2018) present a high resolution body-wave tomography of the whole mantle column beneath the

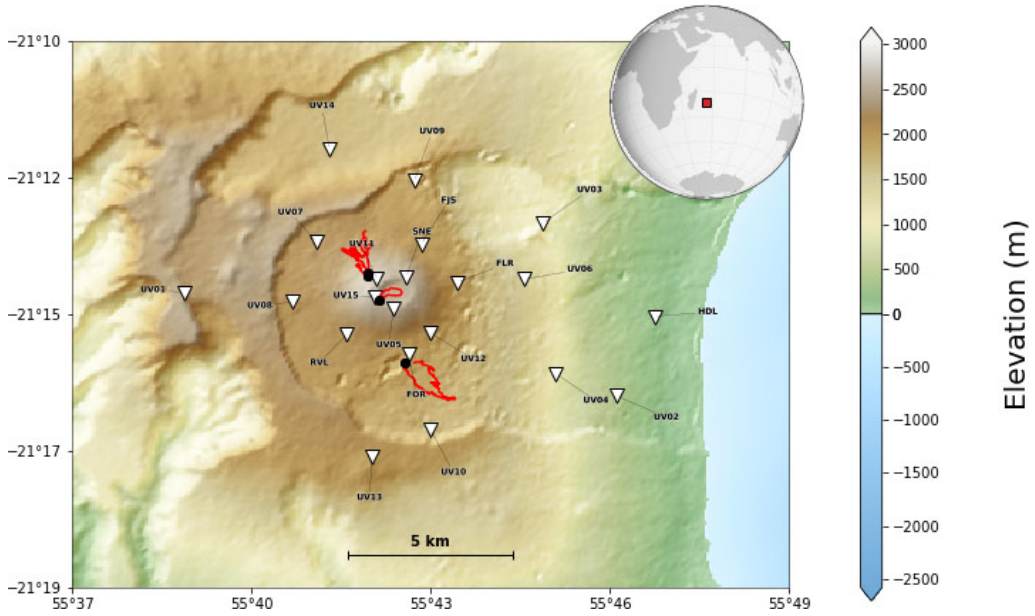

Figure 1: Color shaded relief map of the Piton de la Fournaise volcano, located on the southeast part of La Réunion island. The top right inset shows the location of La Réunion island in the Indian Ocean. Seismic stations used in this study are represented with white inverted triangles. Black dots stand for the position of the eruptive fissures corresponding to the January, October and December 2010 eruptions, located at the west part of the summit cone, south flank and northwest flank respectively. Red lines stand for the lava flows associated with these eruptions.

western Indian Ocean providing a more complex view of the plume beneath La Réunion. Their model reveals that the upwelling shows considerable tilt in the lower mantle instead of being near-vertical and splits into branches near the surface.

The Piton de la Fournaise volcano (PdF) is an intraplate shield basaltic volcano of Hawaiian type located in the southeast part of the island. It is 2631 m high and active since about 530 ka. Throughout its existence, this volcano has been marked by the formation of successive concentric calderas, the latest being the Enclos Fouqué, formed about 4500 years ago (Bachèlery, 1981), in which there is a summit cone of 400 m high and 3 km wide at its base with two craters: the Bory crater and the Dolomieu crater, this latter being the most active one.

The PdF is considered as one of the most active volcanoes in the world, with approximately one eruption occurring every 9 months in average. Thus, its very frequent eruptions weakly dangerous for the population (97% of the recent eruptions occured within the uninhabited caldera) make it an ideal natural laboratory to study active volcanic processes.

Geodetic and seismic data suggest the presence of a shallow magma reservoir around 2500 ± 1000 m below the PdF summit craters (Staudacher et al., 2016). However, the exact geometry of storage zones and their possible inter-connections are still debated. While Lénat and Bachèlery (1990) suggested the presence of small magma pockets scattered between the summit and the sea level, Peltier et al. (2008) inferred from geodetic data a single magma reservoir located above the sea level, regularly recharged by a deeper source.

Since the installation of the volcano observatory of PdF (Observatoire Volcanologique du Piton de la Fournaise - OVPF) in 1979, the seismic network has evolved from a small number of short period stations recording on a triggered basis, to a modern network combining broadband and short period sensors and recording continuously (Battaglia et al., 2016). In 1999, there were 19 short period stations in the network, mostly installed near the summit and around the volcano. In May 1999, the continuous recording appeared with storage on CD-ROMs and the network was completed after the 2007 Dolomieu crater collapse, including up to six broadband 3-component stations by the middle of 2009. Since October 2009, 15 broadband stations located on the volcano were installed as part of the Understanding Volcano project (UnderVolc) (Brenguier et al., 2012; Brenguier, 2014), in addition to the existing seismic network. Figure 1 shows the 21 broadband 3-component stations present in 2010 that we use in this study.

3 Tremor of Piton de la Fournaise volcano

The PdF volcanic tremors are generally co-eruptive, starting when the eruption begins, and disappearing at the end. It is characterized by a relatively broad spectrum around 0.5-10 Hz (Battaglia & Aki, 2003).

The signals generated by seismo-volcanic tremors are generally emergent, without any clear onset. This implies a lack of seismic phase identification and prevents the use of traditional strategies for tremor source location. Therefore this is necessary to develop new methods better suited for its analysis. Battaglia and Aki (2003) proposed a method based on seismic amplitudes for locating events. They showed that once corrected for station sites

effects using coda site amplification factors, the spatial distribution of amplitudes shows smooth and simple contours for events including LP events and eruption tremor. Following this approach, Battaglia et al. (2005b) located sources of several co-eruptive seismic tremors at the PdF and found that they better correlated with the position of the eruptive vents for the 5-10 Hz band, suggesting a generation directly located at the eruptive site. While for frequency above 1.5 Hz, the tremor sources are generally found at shallow depth, they suggest that lower frequencies could be related to deeper processes rather than directly by the eruption observed at the surface. Taisne et al. (2011) used a similar method to study the PdF pre-eruptive seismic crises.

4 Tremor analysis methods based on inter-components cross-correlations

Most of volcano observatories monitor volcanic tremor in real-time based on measuring their amplitudes at a single reference station located near the volcano (e.g., Endo & Murray, 1991). The idea of this approach is that the position tremor source remains more-or-less stable in time and that the amplitude of the seismic signal can be considered as a proxy of the intensity of the tremor generating processes. This single station/component approach can be developed further with using the spectral shape of the signal (instead of its averaged amplitude) leading to a better discrimination of different phases of tremor (Unglert & Jellinek, 2015; Unglert et al., 2016). One of the main difficulties of single component approaches is that they cannot be used to get information about the spatial location and extent of the source. In particular, this might result in difficulties with distinguishing tremors from other types of processes leading to increased seismic amplitudes such as, for example, meteorological and anthropogenic noises.

In this paper we systematically use and compare methods based on correlation of signals recorded at different components. By different components we mean either records made at different positions or different polarities (i.e., vertical, North, East) of a single receiver. We first describe the data pre-processing used in all analyses considered in this paper. Then, we introduce a single-station method aimed at detecting long-acting sources based on stability of inter-components cross-correlations. In a next step, we consider methods based on simultaneous analysis of the whole network of receivers. Our approach is different from the antenna-type detection of tremors based on small-aperture arrays and plane-wave approximation for measuring slowness and azimuth of incoming wave (e.g., Goldstein & Chouet, 1994; Métaxian et al., 2002; Haney, 2014). We rather consider a geometry when

the source of seismic radiation is located within the network. In this case, it has a strong imprint on inter-stations cross-correlations e.g., N. M. Shapiro et al. (2006); Ballmer et al. (2013); Droznin et al. (2015). In volcanic environments these cross-correlations can be used to detect seismic tremors and to locate their source. Here we apply two network-based methods. First, we follow the approach of Droznin et al. (2015) that backproject the cross-correlations envelops in time. Second, we use the representation of ensemble of inter-stations cross-correlations in terms of network covariance matrix suggested by Seydoux, Shapiro, De Rosny, et al. (2016); Seydoux, Shapiro, de Rosny, and Landes (2016); Seydoux et al. (2017) and used by Soubestre et al. (2018, 2019) to study volcanic tremors.

4.1 Data pre-processing

We are focusing on the information contained in the time-variations of the signal phase differences between stations. We also consider the instrument response of the seismic stations to be stable over time and, therefore, do not consider instrument correction. We then further apply the pre-processing usually performed in ambient-noise interferometry (e.g., N. Shapiro & Campillo, 2004; N. M. Shapiro et al., 2005; Bensen et al., 2007).

The data are stored in 24-hours-long time-series in SAC down-sampled from 100 to 20 samples per second. We apply demeaning, linear detrending and bandpass filtering between 1 and 10 Hz. Then, a spectral whitening is applied followed by a temporal normalization according to Seydoux, Shapiro, De Rosny, et al. (2016) such as:

$$u^W(f) = \frac{u(f)}{\langle\langle |u(f)| \rangle\rangle_{df}} \qquad u^N(t) = \frac{u^W(t)}{\langle\langle |u^W(t)| \rangle\rangle_{dt}}. \tag{1}$$

Spectral whitening operation acts to limit the degradation caused by persistent monochromatic sources. It is performed by dividing the signal spectrum $u(f)$ by a smooth version of its amplitude $\langle\langle |u(f)| \rangle\rangle_{df}$. Here we used $df = 0.33Hz$ to compute the running average of $|u(f)|$, the real absolute value of the spectrum. Then the temporal normalization is applied in time domain in order to reduce the effects on cross-correlations of earthquakes and strong local non-stationary noise sources. This is done by dividing $u^W(t)$, the real part of the inverse Fourier transform of $u^W(f)$ (the whitened signal in frequency domain) by a dt-long running average of $|u^W(t)|$. In our case we used $dt = 0.25s$.

4.2 Detection of tremors based on stability of inter-components cross-correlations at a single station

Let us consider a wavefield generated by a tremor source that remains at the same location and with a constant source mechanism. As argued by Droznin et al. (2015); Soubestre et al. (2018), the cross-correlation of such a wavefield between two receivers will remain stable in time and can be used as a "fingerprint" of this particular source. This principle also holds for a cross-correlation between two components of the same receiver and we use this property to design a simple single-station tremor detector. We start with computing inter-components cross-correlations $CC_{i,j}$ $(i, j = E, N, Z)$ in moving windows of length Δt and shifted by $\Delta t/2$. We then compute correlation coefficients between cross-correlation waveforms from consecutive time windows and take the mean value of 6 consecutive computations. The obtained functions $cc^6_{i,j}$ provides us with estimation of the stability of the cross-correlation waveforms that, in turn, is related to existence of stable tremor source. In our case we use moving windows of length $\Delta t = 200$ s to compute inter-components cross-correlations and therefore the $cc^6_{i,j}$ functions correspond to a short-term estimation of the cross-correlation waveforms stability over 700 s. The $cc^6_{i,j}$ function is represented in the part 5.1. We observe that we can detect the three periods of volcanic tremor activity by using only one components pair of a single seismic station. In order to improve the volcanic tremor detection results, we can first average the three $cc^6_{i,j}$ functions obtained from the three components pairs of one single station, and then average the previous functions on several stations.

4.3 Network response function: 2D back-projection of inter-stations cross-correlations envelopes

We follow the approach of (Droznin et al., 2015) who developed a 2D source-scanning algorithm based on the stacks of inter-stations cross-correlations envelopes, in order to detect volcanic tremors and to locate their sources. This method is based on an assumption that tremor source is relatively shallow and that seismic energy propagates toward the stations along the surface. The differential travel times of signals emerging in inter-stations cross-correlations are then interpreted in terms of surface wave (2D) propagation in order to find the geographical location of the tremor source. The location is done by performing a 2D grid search with tested sources spaced 500 meters apart. We first compute the inter-stations

cross-correlations (we only use the vertical component seismograms) between all pairs of available stations and when data from the 21 stations are available. We therefore end up with 210 pairs of cross-correlations. The next step consists in computing the smoothed envelopes of the cross-correlation waveforms. This is done by computing the absolute value of the analytic signal derived from the Hilbert transform and by performing a convolution with a 6 s long Gaussian window. Then, for every tested source position we compute travel times for all stations using an estimated horizontal wave propagation velocity of 600 m/s. This velocity was estimated by performing a linear regression between the maxima of the smoothed cross-correlations envelopes as seen in Figure 2. This figure represents the smoothed cross-correlations calculated between the UV05 station (the closest available station to the January eruptive center) and all the others available stations for the day 03.01.2010. The red line is the result of the linear regression whose slope corresponds to a horizontal wave propagation velocity of 600 m/s. We observe similar velocities for other days with volcanic tremor activity.

Such a weak propagation velocity is consistent with wave propagation in near-surface layers constituted of poorly consolidated volcanic materials. Each cross-correlation envelop $S^{i,j}$ is shifted by the time difference needed for the wave to travel from the tested source to the two stations i and j and we finally compute the network response $R(r)$ by stacking at zero lag time the value of the shifted envelopes for all stations pairs as:

$$R(r) = \sum_{i=1}^{N} \sum_{j=i+1}^{N} S^{i,j}[t^i(r) - t^j(r)] \tag{2}$$

with N the number of stations, r the source position and $t^i(r)$ the travel time between the tested source and the station i.

This network response characterizes the likelihood of location of a seismic source in a particular position. In order to better visualize the location result, a normalized network response is computed

$$\tilde{R}(r) = \frac{R(r) - R^{min}}{R^{max} - R^{min}} \tag{3}$$

with R^{max} and R^{min} are the absolute maximum and minimum of $R(r)$. Locations of tremor obtained with this method are shown in part 5.2. Finally, we calculate the normalized maximum network response

$$\tilde{R}^{max}(n) = 100 \times \frac{R^{max}(n) - R^{min}(n)}{R^{ref}} \tag{4}$$

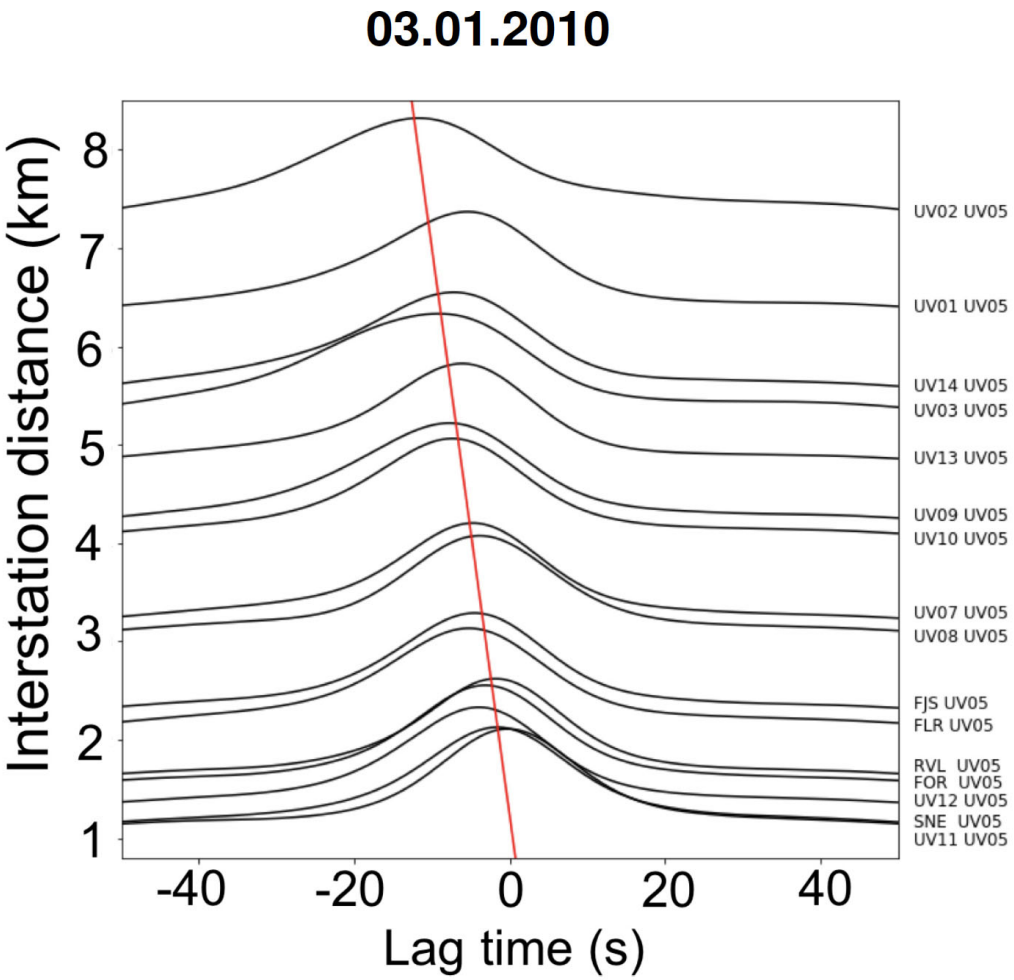

Figure 2: Smoothed cross-correlations of vertical component records between UV05 station and other available stations during the second day of the January eruption associated with a continuous volcanic tremor. The red line corresponds to the result of a linear least-squares regression between the smoothed cross-correlations maxima, giving an apparent velocity of 600 m/s.

for every day of the 2010 year in order the compare their values, where n is the day number and R^{ref} a normalization coefficient chosen as an average of $R^{max} - R^{min}$ over the October 2010 eruption, the longest period of tremor activity during the year. The obtained detection results are shown in section 5.1.

4.4 Covariance matrix analysis

Detection of coherent tremor signals: We use the method proposed by Seydoux, Shapiro, De Rosny, et al. (2016) when an ensemble of inter-stations cross-correlations computed in a frequency domain can be represented with the network covariance matrix. This matrix being inherently Hermitian and positive semidefinite, it can be decomposed on the basis of its eigenvectors associated with real positive eigenvalues. The main idea behind this method is to consider that the number of independent signals can be deduced from the rank of the covariance matrix (number of non-zero eigenvalues), with the largest eigenvalues corresponding to these signals and the smallest to the background noise. A single source would generate a rank 1 covariance matrix, and this rank would increase with the number of independent sources. However, the number of independent sources can not be directly obtained from the rank because of the presence of seismic noise (generated by ocean microseismic, wind, etc) and instrumental electronic noise. In addition, as the covariance matrix is estimated from a finite number of windows, this may reduce the ability to capture the independent seismic signals. Nevertheless, the width of the covariance matrix eigenvalues spectrum ($\sigma(f)$ called spectral width) can be used as a proxy for the number of independent seismic sources (Seydoux, Shapiro, De Rosny, et al., 2016). Thus, this spectral width is high when it corresponds to ambient seismic noise produced by distributed sources, while it is low when it corresponds to a spatially coherent signal produced by a single localized source, such as volcanic tremor.

The covariance matrix is defined as :

$$\Gamma(f) = E[\boldsymbol{u}(f)\boldsymbol{u}^{\dagger}(f)], \tag{5}$$

where $\boldsymbol{u}(f) = [u_1(f), u_2(f), ..., u_N(f)]^T$ is the array data vector from the records of N seismic stations, † stands for the Hermitian transpose, so the outer product $\boldsymbol{u}(f)\boldsymbol{u}^{\dagger}(f)$ is an $N \times N$ matrix and E represents the expected value. We start by cutting the signal day into a number of overlapping time windows that we call averaging windows in which the spectral whitening and temporal normalization (equations 1) are applied following Seydoux,

Shapiro, De Rosny, et al. (2016). Then, each averaging window is cut into M overlapping subwindows of length δt such that $\Delta t = Mr\delta t$, where Δt is the length of the averaging time window and r the overlapping ratio that is 0.5 on our case. We apply a taper on the data prior to calculate the Fourier transform on the subwindow to avoid sharp windows, that is why the signal segments are overlapped with a factor of 50 % in order not to loose any information located in consecutive windows. Then we compute the cross-spectra matrices in each subwindow and the covariance matrix $\boldsymbol{C}(f)$ is calculated by averaging over the M subwindows such as:

$$\boldsymbol{C}(f) = \langle \boldsymbol{u}(f)\boldsymbol{u}^{\dagger}(f)\rangle_{\Delta t} = \frac{1}{M}\sum_{m=1}^{M} \boldsymbol{u}_m(f)\boldsymbol{u}_m^{\dagger}(f), \tag{6}$$

with $\boldsymbol{u}_m(f)$ the data Fourier spectra vector in the subwindow m. To make the calculation on the whole year 2010, we chose $M = 50$ and $\delta t = 40$ s. We note that δt must be long enough for the tremor seismic wave to have time to propagate through the entire network. We thus obtain 1000 s long windows that overlap with a 50 % factor. The obtained covariance matrix is Hermitian and positive semi-definite, so it can be decomposed on the basis of its complex eigenvectors $\boldsymbol{v}_n$ associated with real positive eigenvalues λ_n:

$$\boldsymbol{C}(f) = \sum_{n=1}^{N} \lambda_n \boldsymbol{v}_n \boldsymbol{v}_n^{\dagger}. \tag{7}$$

Then eigenvalues are arranged in decreasing order and the covariance matrix spectral width is computed as a function of frequency as:

$$\sigma(f) = \frac{\sum_{i=1}^{N}(i-1)\lambda_i(f)}{\sum_{i=1}^{N}\lambda_i(f)}. \tag{8}$$

Location of tremors from the covariance matrix first eigenvector: This location method (described in Soubestre et al. (2019)) is similar to the 2D source-scanning algorithm described in the part 4.3 but here we focus on the dominant wavefield and we use a grid search on a 3D space grid to determine the geographical position together with the depth of the dominant tremor source. To do that, we focus on the first eigenvector of the network covariance matrix containing information about the location and the mechanism of the dominating tremor source. The first eigenvector represents the most coherent part of the wavefield and acts as a de-noising operator (Soubestre et al., 2019).

The filtered covariance matrix $\tilde{\boldsymbol{C}}(f)$ is obtained from the complex outer product of the first eigenvector $v_1(f)$ with himself :

$$\tilde{\boldsymbol{C}}(f) = v_1(f)v_1^{\dagger}(f). \tag{9}$$

Then, the time-domain filtered cross-correlations are retrieved by performing the inverse Fourier transform of $\tilde{\boldsymbol{C}}(f)$, and smoothed to obtain their envelopes, as explained in the previous section. After the smoothing, each cross-correlation envelope is shifted by the time difference between travel times from every tested point of the 3D grid to the two considered stations. The Network Response Functions (NRF) are then obtained by stacking the value at zero lag-time of shifted cross-correlations envelopes. These NRF are then normalized using equation (3) (and called likelihood afterwards) to visualize the most likely source position corresponding to the function maximum in space.

5 Results

5.1 Detection of tremors and other types of seismic activity

Figure 3a shows the result of the $cc^6_{i,j}$ function (described in section 4.3) for the N - Z components pair of station UV12. We note that we can detect the three eruptive tremors (highlighted in red in the figure) only with one components pair of a single station. We can then improve these detection results by averaging the three $cc^6_{i,j}$ functions obtained from the three components pairs and we show an example for the UV12 station in the Figure 3b. In order to improve the signal-to-noise ratio we perform an average over several stations. We show in Figure 3c the result averaged over 12 stations (36 components) whose continuous records without significant interruption are available through the whole year 2010. We represent some zoom of this station-averaged $cc^6_{i,j}$ function in Figure 7c, 8c and 9c. In addition to the volcanic tremors and to their preceding seismic swarms, we can also detect high values of the function in Figure 3c the 23.09.2010 (corresponding to the day 266) where a dyke intrusion occurred without leading to an eruption (Roult et al., 2012).

Figure 4a shows the normalized maximum 2D network response (equation 4) computed every day (time resolution similar to Droznin et al. (2015)). This allows us to detect the January and October volcanic tremors and we also observe an increase of the NRF values since the beginning of September (day 244) corresponding to an increase in the seismicity prior to the October eruption. However we can not detect the December tremor here because of the temporal resolution. Figure 4b shows the same function computed with an shorter time resolution, i.e., in 1000 s long time windows. We can now detect the three tremors (see the zoom of spectral width and network response function in Figures 7, 8 and 9) and we also observe that $\tilde{R}^{max}$ becomes more sensitive to the high-seismicity period. Indeed, high

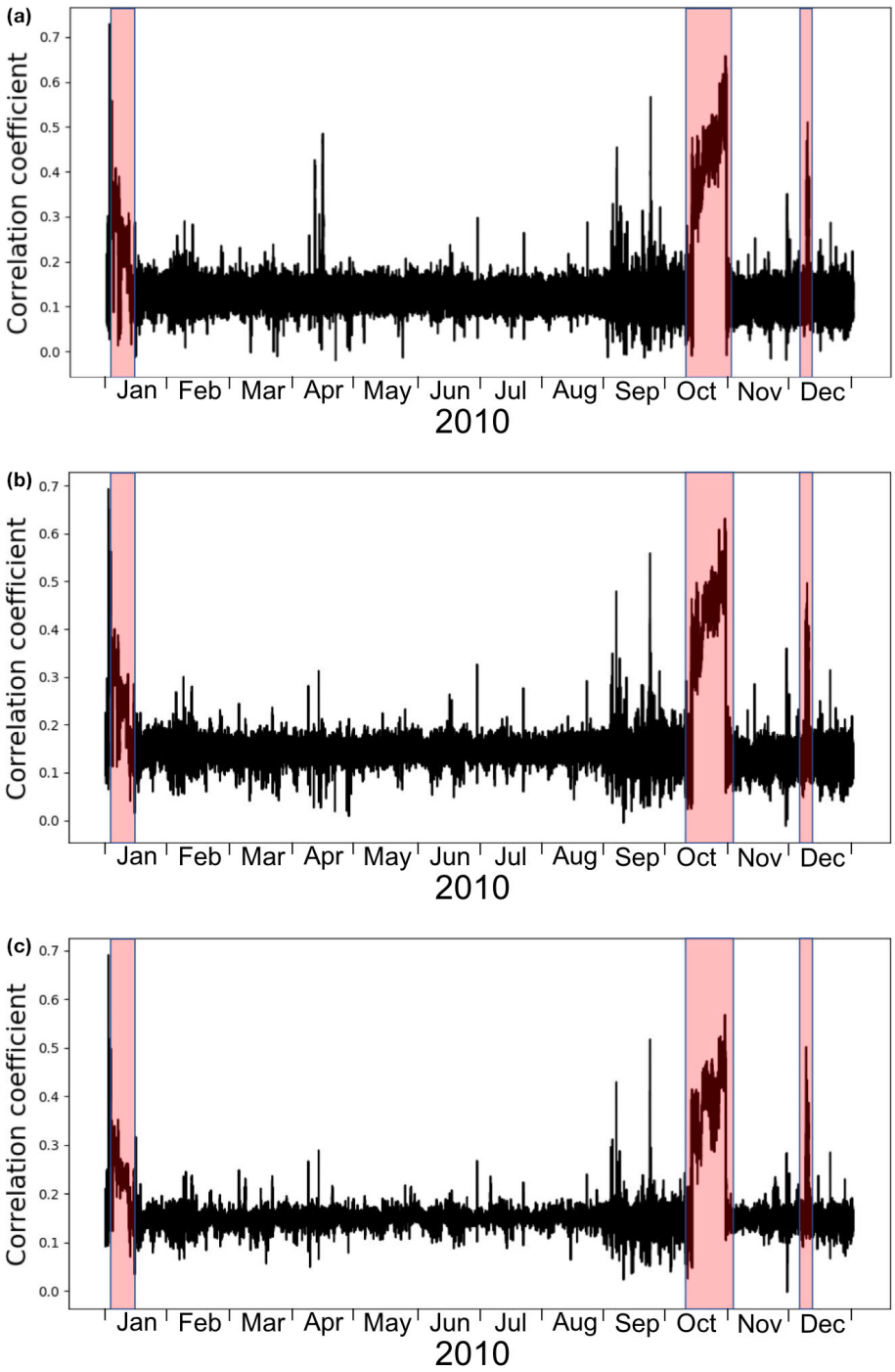

Figure 3: Tremor detection from inter-components cross-correlations at a single station. (a) Correlation coefficient function $cc^6_{i,j}$ computed for the N - Z components pair of the UV12 seismic station. The red areas highlight the January, October and December tremors. (b) Average of the three correlation coefficient functions $cc^6_{i,j}$ obtained for the three components pairs of the UV12 seismic station. The red areas highlight the January, October and December tremors. (c) Average of the averaged function represented in (b) on 12 seismic stations whose data availability is stable and identical over the 2010 year (UV01 to UV14, without UV04 and UV06).

values are observed for the pre-eruptive seismic crises corresponding to each eruption and for the whole month of September.

Figure 4c shows the covariance matrix spectral width (equation 8) computed on 1000 s long overlapping time windows for every frequency, this can be seen as a time-frequency representation of the wavefield recorded by the whole network highlighting the coherent signals. Figure 4d represents the average of this spectral width on the frequency-band 1-5 Hz. This function represents another network-based detector and all three tremors can be identified with lower values of the spectral width. We note that while the computation of $\tilde{R}^{max}$ requires an a-priori on the medium velocity, there is no a-priori for the spectral width calculation. Despite this, the two network-based methods result in a similar first-order information and we observe an anti-correlation when tremor sources produce high value of $\tilde{R}^{max}$ and low value of $\sigma(f)$.

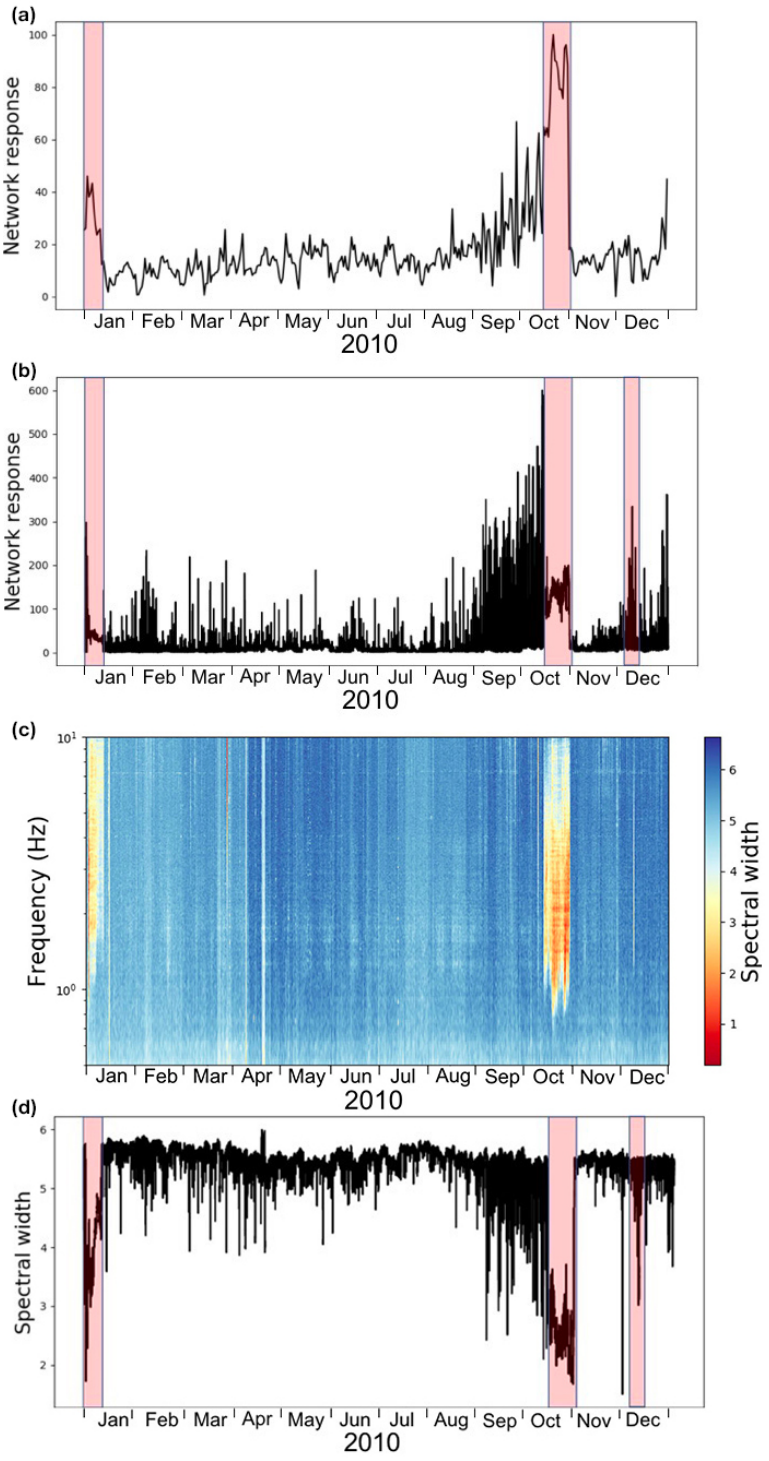

Figure 4: Tremor detection from inter-stations cross-correlations. (a) Network response function $\tilde{R}^{max}$ (equation 4) computed every day. The red areas highlight the January and October tremors. (b) Network response function $\tilde{R}^{max}$ computed on 1000 s long time windows. (c) Covariance matrix spectral width computed for every frequency on overlapping 1000 s long time windows. (d) Average of the covariance matrix spectral width in the frequency band 1-5 Hz. In order to limit the impact of the missing stations on the functions (a), (b) and (c), we normalize them by the number of functional stations for each day.

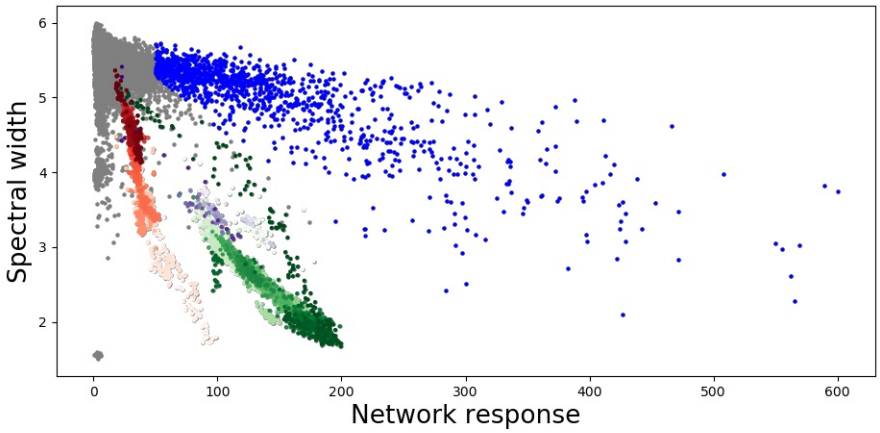

Figure 5: Average spectral width as a function of the network response function $\tilde{R}^{max}$. Colors correspond to different clusters of events. The three tremors are represented with color gradations from lightest to darkest in order to observe their evolution over time. Red colors stand for the January tremor with corresponding network response and spectral width represented in Figures 7a and 7b respectively. Green colors stand for the October tremor as represented in Figures 8a and 8b. Purple colors stand for the December tremor (see Figures 9a and 9b). Blue colors stand for the earthquakes occurring during the 2010 year and especially prior and during the pre-eruptive seismic crisis.

A more detailed comparison of two network-based methods is shown in Figure 5 that represents the average spectral width as a function of the network response function $\tilde{R}^{max}$. We can see different trends corresponding to clusters of different seismic events. This allows to clearly differentiate the January and October volcanic tremors represented by red and green colors respectively, as the January tremor is characterized by lower values of the network response function (see also Figures 7a, 7b, 8a and 8b). December tremor can also be seen in Figure 5 with purple colors, with similar values of the network response function but higher values of the average spectral width than the October tremor (see also Figure 9a and 9b). We notice that we can thus separate the summit tremor (occurring in January) from the two flank tremors occurring in the South and North-West flanks in October and December, respectively. We also observe a different temporal evolution for the January and October tremor. January tremor is characterized by very low values of spectral width at the beginning of the eruption (very light red in Figure 5) and it evolves until reaching values equivalent to that of seismic noise (dark red in Figure 5). Conversely the October tremor

begins with intermediate values of spectral width (very light green in Figure 5), then it ends with very low spectral width values (dark green in Figure 5) and finally the spectral width becomes higher and higher until the eruption is completely over.

Another trend is distinguishable in Figure 5 with more scattered points represented in blue which correspond to the earthquakes occurring during the 2010 year and especially prior and during the pre-eruptive seismic crisis. We also observe high values of the network response function at the end of the year that are followed by an increase of the micro seismicity under the summit since the beginning of the year 2011 (OVPF, 2011). Grey points in the top left corner of Figure 5, characterized by low values of network response and high values of average spectral width, correspond to seismic noise during the whole year. We also note a few points on the bottom left of the Figure 5, characterized by very low values of the average spectral width, that correspond to a few hours in the end of November where there was a technical problem and several stations were down.

Finally, we can also make a 3-D comparison between the station-averaged $cc^6_{i,j}$ function (whose zoom during eruptions are shown in Figures 7c, 8c and 9c), the NRF and the spectral width as seen in Figure 6. Before comparing all the three functions, we re-calculated the NRF and the spectral width with 200 s long overlapping windows and we computed a moving average between 6 consecutive windows. In addition to the separation between summit and flank tremors, we can also distinguish some points colored in orange corresponding to an intrusion occurring for a few hours on 23.09.2010 (Roult et al., 2012). Here the blue points correspond to the three pre-eruptive seismic swarms that we can clearly distinguish from the seismo-volcanic tremors.

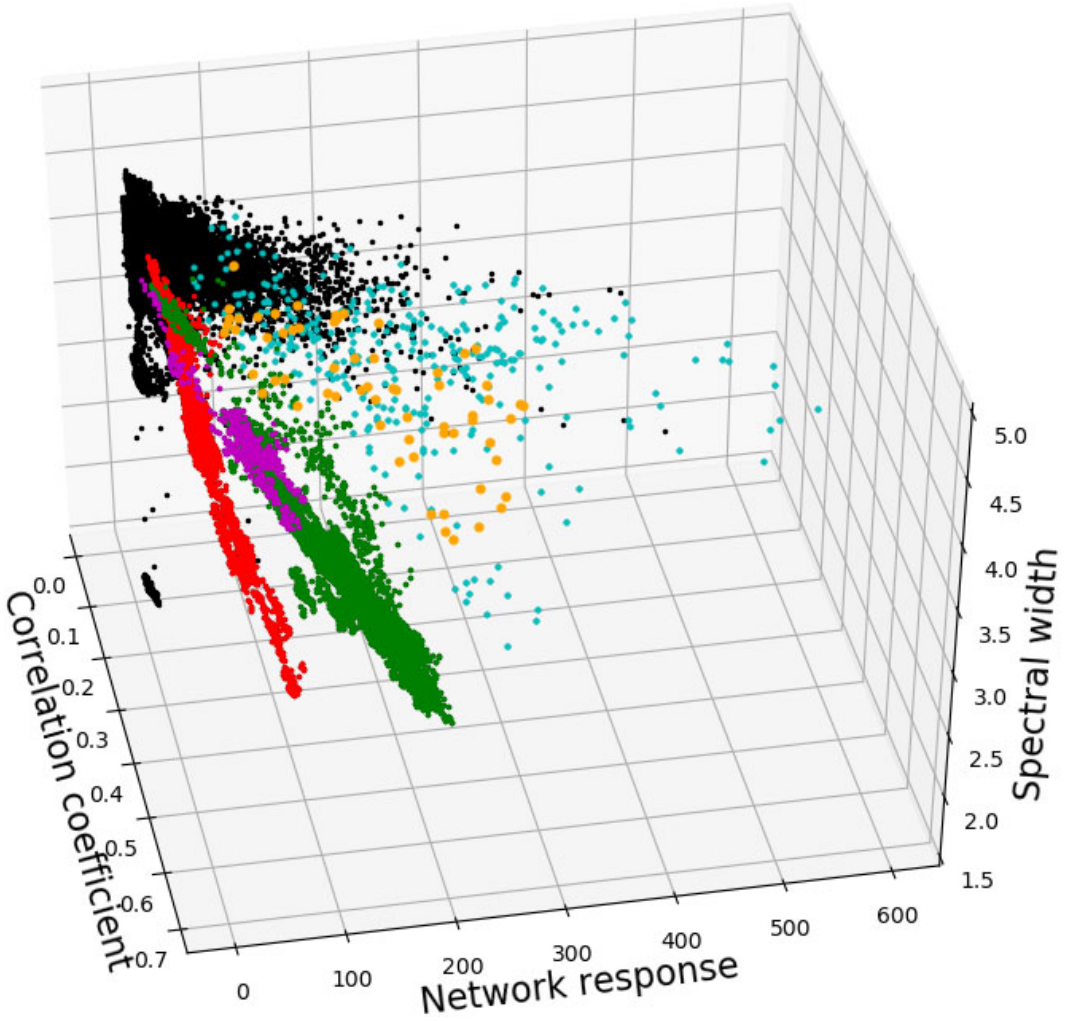

Figure 6: 3D comparison between the station-averaged $cc^6_{i,j}$ function labeled as "correlation coefficient", the NRF and the average spectral width. The January, October and December tremors are represented by red, green and magenta colors respectively. The orange color stands for the dyke intrusion occurring in September and the blue color stands for the January, October and December pre-eruptive seismic crises.

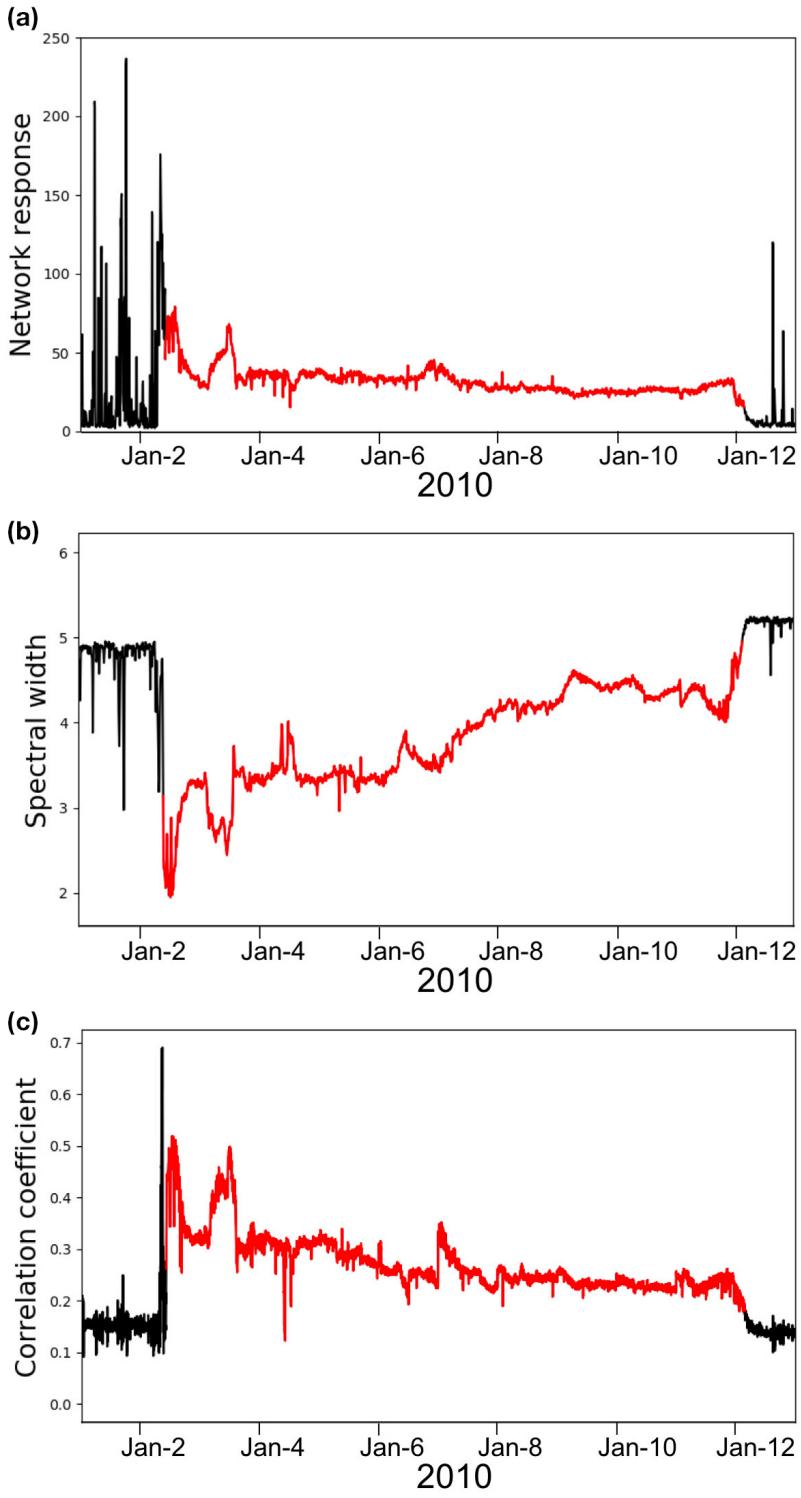

Figure 7: Zoom on the January eruption and its pre-eruptive seismic swarm for (a) the NRF, (b) the spectral width and (c) the station-averaged $cc^6_{i,j}$ coefficient correlation function. The red color stand for the January volcanic tremor activity.

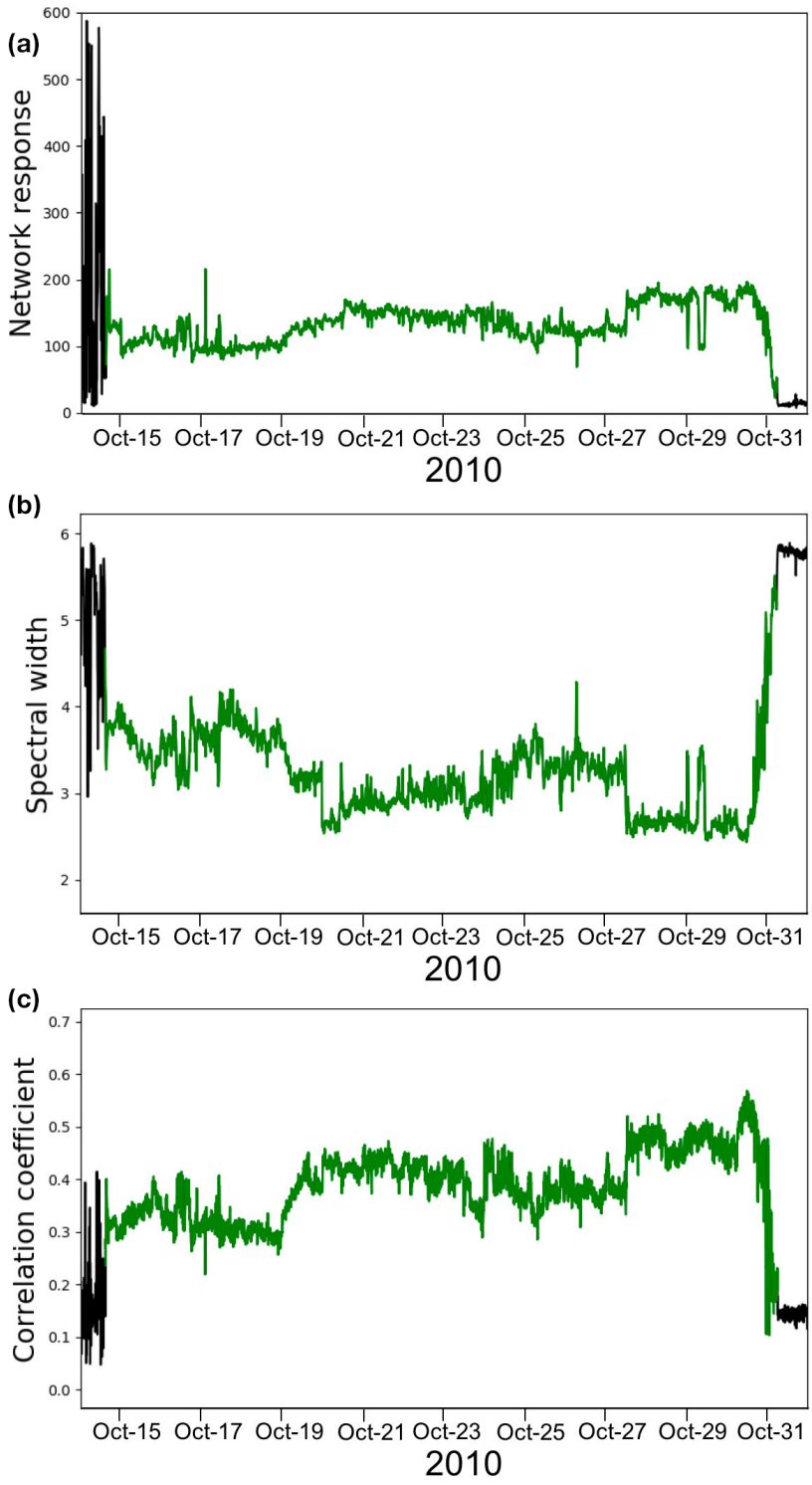

Figure 8: Zoom on the October eruption and its pre-eruptive seismic swarm for (a) the NRF, (b) the spectral width and (c) the station-averaged $cc^6_{i,j}$ coefficient correlation function. The green color stand for the October volcanic tremor activity.

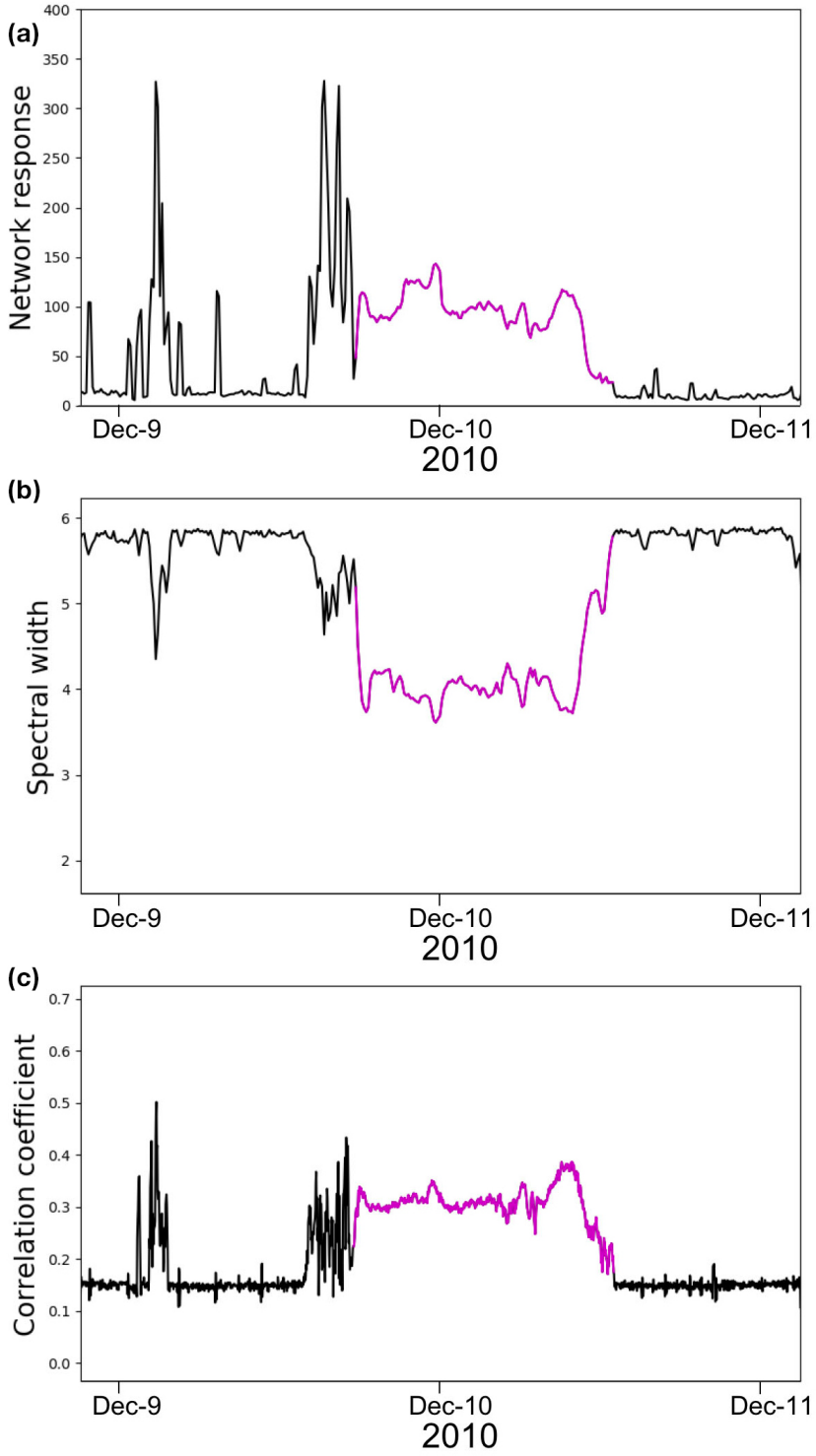

Figure 9: Zoom on the December eruption and its pre-eruptive seismic swarm for (a) the NRF, (b) the spectral width and (c) the station-averaged $cc^6_{i,j}$ coefficient correlation function. The magenta color stand for the December volcanic tremor activity.

5.2 Location of tremor sources

Figure 11 shows the tremor sources location results in 2D using a horizontal wave propagation velocity of 600 m/s for one day of the January eruption (11a), one day of the October eruption (11b) and the 15 hours of the December eruption (11c). We observe a distinct location of the tremor source for each eruption, corresponding quite well with the eruptive sites represented as a black dot for each case.

This is now interesting to compare these results of the 2D source scanning algorithm with a 3D location based on extraction of the dominant wavefield (as explained in the part 4.4). For this comparison, we calculate the daily covariance matrix by setting $M = 50$ and $\delta t = 40$ s to end up with 1000 s long windows that overlap with a 50% factor. For this 3D location we consider that tremors and their cross-correlations are dominated by S waves (Soubestre et al., 2019). An S wave velocity model is therefore needed to predict the inter-stations travel time differences. For simplicity, in this study we use a constant S wave velocity V_S. We fix $V_S = 1500$ m/s here, which corresponds approximately to the average S wave velocity in the 2500 m volcanic edifice (Mordret et al., 2015), where most of the seismic sources we are interested in are located. Then we test different values of the Gaussian window width used to smoothed the cross-correlations reconstructed from the first covariance matrix eigenvector. We make our tests on four hours of the day 15.10.2010 during the October tremor between 15h and 19h, when inter-components cross-correlations remain stable. We thus stack the obtained cross-correlations computed in 1000 s windows during these four hours. We compute their envelopes by testing different values of Gaussian window width and normalize them by their maxima. We then perform a 3D back-projection of these obtained cross-correlations envelopes and compute the likelihood function for each tested value of the Gaussian window width. We show in Figure 10 the maximum likelihood value as a function of the Gaussian window width. We chose a Gaussian window width value of 1.5 s, corresponding to the corner of the curve in Figure 10 pointed by the red dashed lines, beyond which the maximum likelihood value no longer increases significantly.

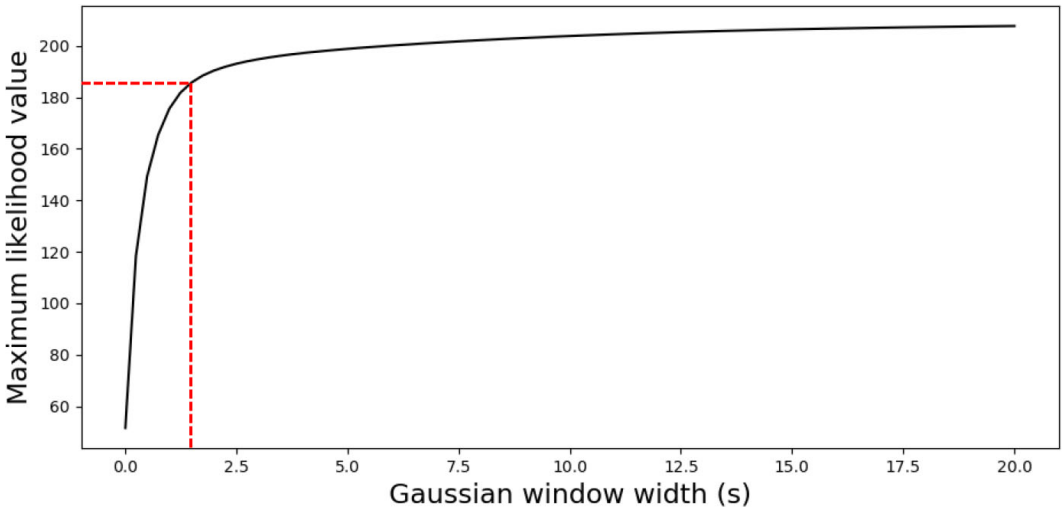

Figure 10: Maximum likelihood value as a function of the Gaussian window width used to smoothed the time-domain filtered cross-correlations. We chose the Gaussian window width value corresponding to the corner of the curve pointed by the red dashed lines.

Figure 12 shows the results of the 3D location for the same time periods as has been shown in 2D (Figure 11) for January (12a), October (12b) and December (12c) tremors. We define a 3D grid with points spaced every 250 m in order to compute the likelihood function that is then normalized using the equation (3). For Figures (12a) and (12b) we stacked the 1000 s overlapping windows for the entire days 03.01.2010 and 15.10.2010, respectively, while we stacked them only for the 15 hours of eruption between the day 09.12.2010 and 10.12.2010 for Figure (12c). We observe that tremor source geographical positions are similar to those obtained in the Figure 11. January and December tremors seem to be located directly under the eruptive fissure while the maximum NRF value associated with the October tremor might be located a few hundred meters under the surface.

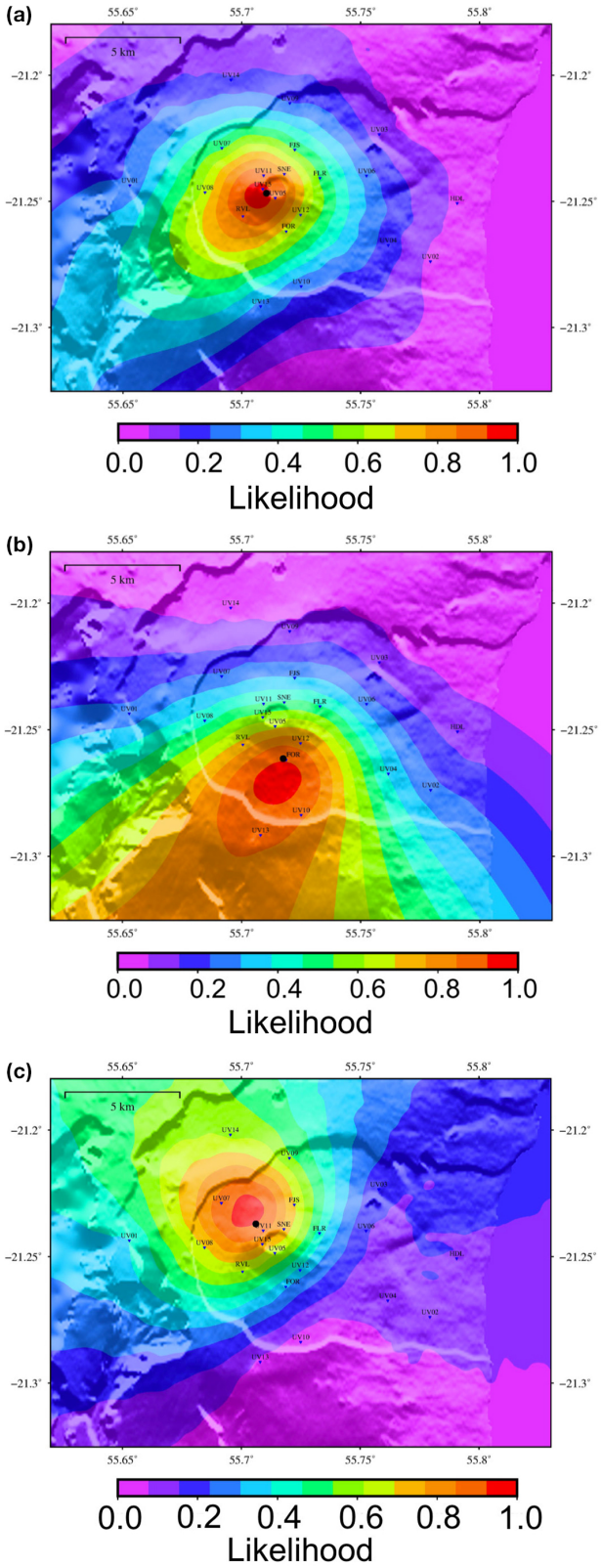

Figure 11: Network response functions $\tilde{R}$ for (a) the day 03.01.2010 (second day of the January eruption), (b) the day 15.10.2010 (second day of the October eruption) and (c) the 15 hours of the December eruption between days 09.12.2010 and 10.12.2010. 2D location are performed assuming a 600 m/s horizontal wave propagation velocity. Black dots stand for the eruptive sites for each eruption.

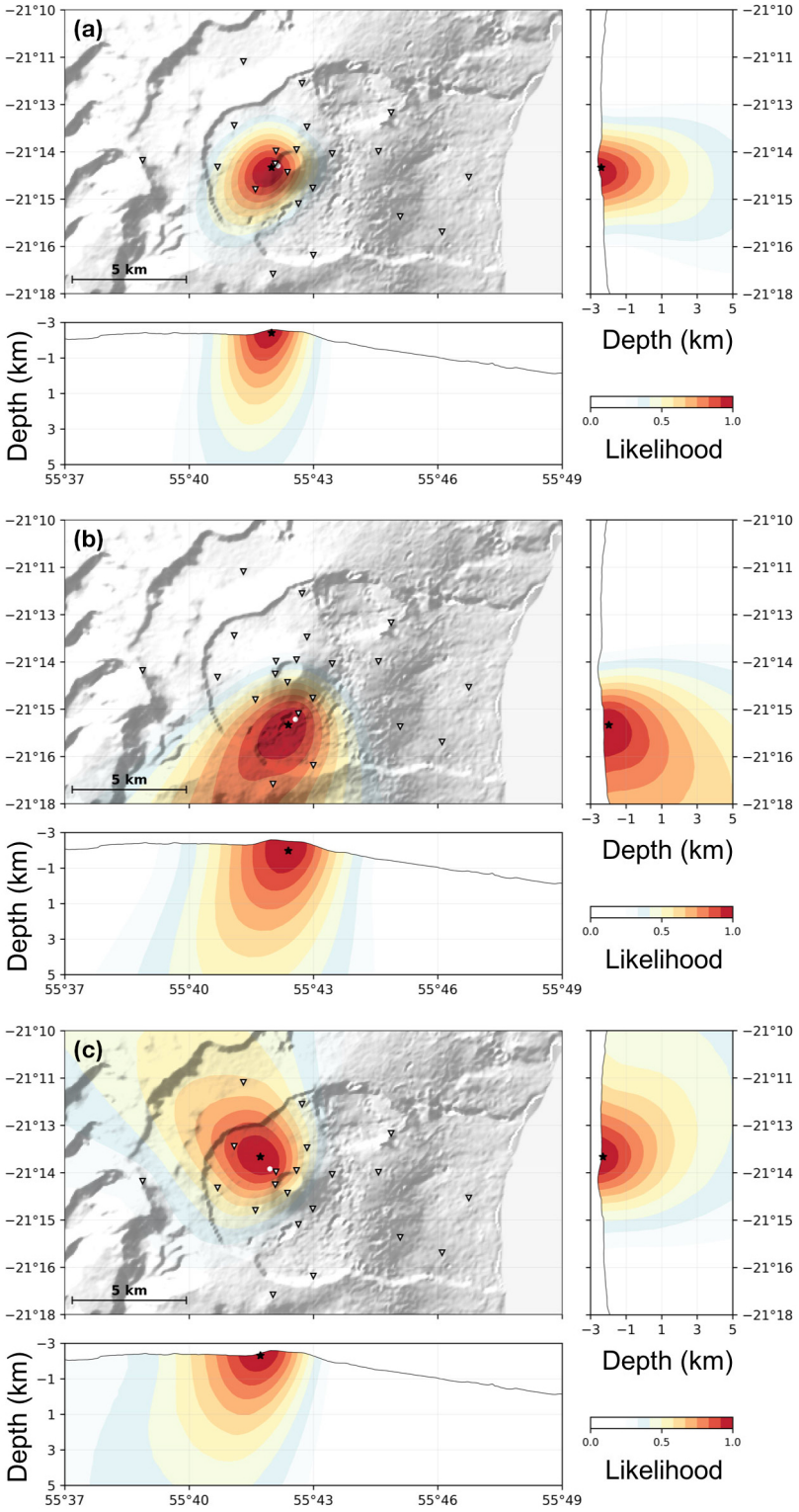

Figure 12: Network response functions (NRF) $\tilde{R}$ calculated from the covariance matrix first eigenvectors for (a) the day 03.01.2010, (b) the day 15.10.2010 and (c) the 15 hours of the December eruption between days 09.12.2010 and 10.12.2010. The black stars stand for the location of the source with the maximal NRF value and the white dot points for the eruptive sites. 3D location are performed assuming a 1500 m/s average S wave velocity in the volcanic edifice.

5.3 Pre-eruptive swarms

To focus on details of volcano-tectonic (VT) events occurring in the observed pre-eruptive seismic swarms we modify the temporal normalization of the data and instead of applying the running absolute mean normalization (described in section 4.1), we divide the traces (once spectral whitening is applied) by their mean absolute deviation (MAD). We also enhance the temporal resolution of the covariance matrix analysis and modified the parameters introduced in the part 4.4, by setting $M = 25$ and $\delta t = 16$ s. As a result, the covariance matrix spectral width is computed in 200 s long overlapping time windows. Figure 13 shows the result of such enhanced seismic event detection and location during the first day of the October eruption (14.10.2010) with pre-eruptive seismic crisis and tremor starting at 15:00. We can clearly distinguish discrete VT events occurring in the seismic crisis in Figure 13a in difference with the continuous following tremor.

Then we perform a 3D location by focusing on the first eigenvector of the covariance matrix computed for this day. We stack 10 consecutive 200 s long overlapping windows, to end up with a location point every 1000 s obtained with using $V_S = 1500$ m/s and a Gaussian window width of 1.5 s. We represent the depth as a function of the latitude in Figure 13b, with the symbol colors corresponding to the windows central times. We observe that events occurring during the seismic crisis are located under the summit dome between $\pm$ 1 km around the sea level which is quite in agreement with what is typically observed for pre-eruptive swarms at PdF. For example Schmid (2011) located VT events from the 14.10.2010 seismic swarms beneath summit crater between 500 m below sea level and 1000 m above sea level. Then the seismicity seems to migrate toward the eruption site in the south flank for October eruption. Using template matching and relocation techniques, Duputel et al. (2019) show a clear correlation between pre-eruptive earthquake locations and the azimuth of eruptive sites which is consistent in our case with the presence of VT earthquakes in the southern branch of the summit cone before the migration. In Figure 13c, the depth is represented as a function of time and we see that when the eruption begins a tremor source appears at shallow depth, close to the eruptive fissure. At the same time, some sources seem to remain close to the sea level after the eruption onset that may correspond to a few co-eruptive VT events.

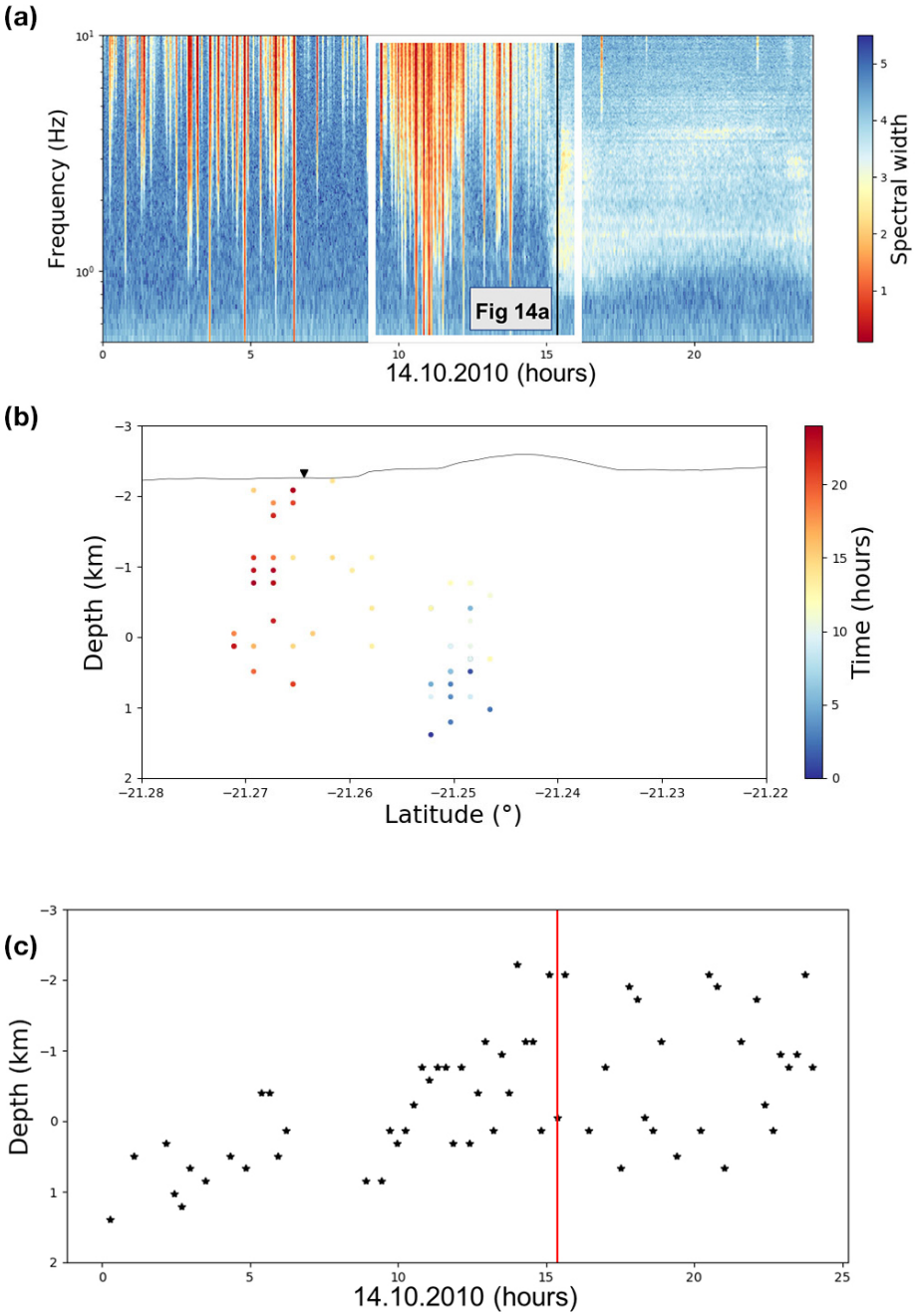

Figure 13: (a): Zoom on the covariance matrix spectral width calculated on 200 s overlapping time windows during the day 14.10.2010, first day of the October eruption. Black line stands for the beginning of the eruption. The white frame corresponds to the zoom represented in the Figure 14a. (b): 3D location of the detected seismic signals on 1000 s time window during the day 14.10.2010, the depth is represented as a function of the latitude with the color representing the windows central times. The black triangle at the surface stands for the eruptive site position. (c): Same location with the depth represented as a function of the time. Red vertical line in (c) stands for the beginning of the eruption.

In Figure 14a, a zoom of the spectral width is represented for the day 14.10.2010 between 09:30 (beginning of the seismic swarm main part) and 16:20 (one hour after the eruption onset). Figure 14b shows an example of a 3D location on a 200 s long window of a VT event occurring at 10:30, situated at the sea level under the summit cone. In addition to the seismic tremor and VT events constituting the pre-eruptive seismic swarm, the computation of the covariance matrix spectral width allows also to detect another type of recently discovered seismic swarm of events characterized by a very high frequency content (called HF swarm) (De Barros et al., 2013). As stated by Roult et al. (2012), the classical sequence of events preceding an eruption at PdF is: a first increase of VT events, a swarm of VT with larger magnitudes, then a seismically quiet or low intensity sequence with small number of VT events linked to magma migration followed by the tremor onset and the eruptive fissure opening. During the quiescent period between the swarm and the tremor, De Barros et al. (2013) identified a swarm of HF events the 14.10.2010 since 13:00, located in the area of the eruptive fracture in the south flank and interpreted as a response of the shallow part of the edifice to the stress changes due to the dike propagation. We can observe in the Figure 14a some coherent signals between the end of the VT swarm and the tremor, in particular from 14:00 to 15:00, for frequencies larger than 3 Hz. We represent in Figure 14c an example of a 3D location on a 200 s long window of a HF event occurring at 14:10. There is therefore a migration of the seismicity from the pre-eruptive seismic swarm under the summit cone at the sea level toward a HF swarm superficially near the future eruptive site more than one hour before the eruption.

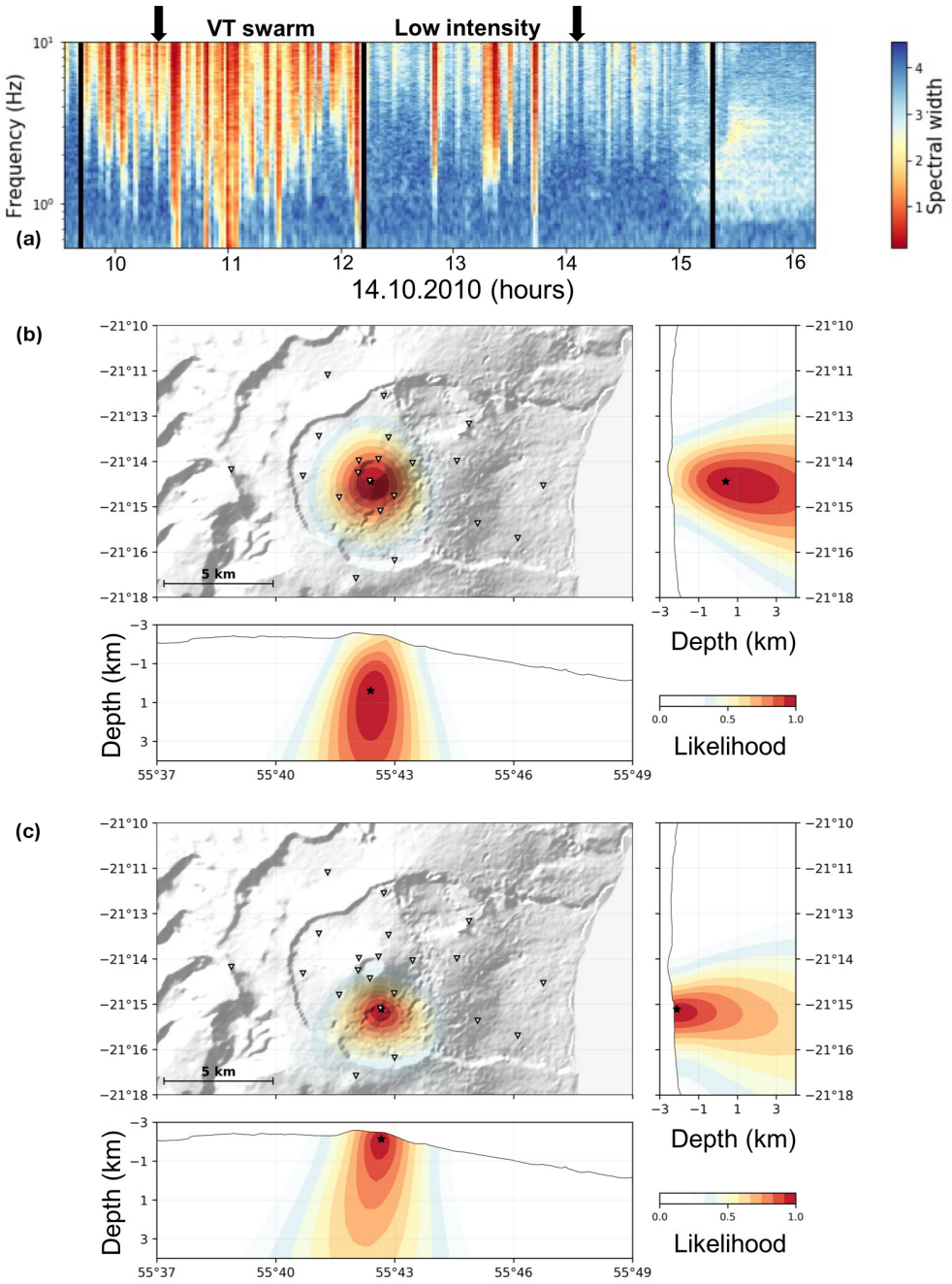

Figure 14: (a) Zoom of the covariance matrix spectral width the day 14.10.2010 between the beginning of the seismic swarm main part (09:30) and one hour after the eruption onset. The two black arrows show the timing of the two events with locations shown in (b) and (c). The two first vertical black lines stand for the beginning and the end of the VT swarm main part. Then there is a phase of low intensity seismicity with a small number of VT events. During this phase the lateral migration of the dike begins and we can observe a coherent high-frequency swarm. The third one marks the onset of the volcanic tremor and associated eruption. (b) Network response functions $\tilde{R}$ calculated from the covariance matrix first eigenvectors, the day 14.10.2010 for a VT event at 10:30 and (c) for a HF event that is part to the high-frequency seismic swarm. These events are located with a velocity of 1500 m/s.

6 Discussion and conclusions

In this paper, we tested methods that use the phase information contained in continuous seismic signals to study seismo-volcanic tremors. First, we introduced a new method of detection of tremors based on stability of inter-components cross-correlations at a single station. In a next step, we systematically compared this new method with two previously proposed network-based methods by applying all three methods to continuous data recorded by stations of the Piton de la Fournaise (PdF) volcano observatory seismic network during 2010. The second method called "network response function" (Droznin et al., 2015) has been applied for the first time to the PdF data. The third method based on the network covariance matrix has been previously applied to the dataset used in this paper by Seydoux, Shapiro, De Rosny, et al. (2016). However, in this previous paper the time resolution of the analysis was relatively low (one day), and here we increased it to be able to detect individual volcanic earthquakes.

All three methods have been demonstrated to be very sensitive to volcanic tremors and detected all three eruptive tremors occurred during 2010. They are also capable to detect strong pre-eruptive seismic swarms. In addition to this, the two network-based methods detect a large number of volcanic earthquakes and, in particular, the significant increase of seismicity during the month preceding the October 2010 PdF eruption as seen in Figure 4. This seismicity increase is well correlated with the measured decrease of seismic velocity that is interpreted to be linked to the volcanic edifice deformation induced by magma pressure build-up and injection (Brenguier et al., 2012).

The "single-station inter-components cross-correlations" method can be implemented on volcanoes monitored by a small number of stations. Among the two network-based methods, the "covariance matrix" detector has some advantage because it does not require a-priori information about the wave propagation velocity. Additional advantage of network based-methods is their ability to locate tremor sources. In the case of a network with significant number of well distributed stations, the 3D location based on "spatially filtered" cross-correlations (reconstructed from dominant covariance matrix eigenvector) can be done. Apart from the seismic data quality, the accuracy of such location depends on the knowledge of the internal velocity structure of the volcano. In this paper, the tests were limited to location with using homogeneous velocity. In principle, wave propagation in 3D velocity models can be easily incorporated. Permana et al. (2019) used a similar method to locate

volcanic tremor using a 1-D S wave model as in Soubestre et al. (2019) (expect that they do not focus on a dominant tremor source by filtering by the first eigenvector of the covariance matrix). They simulate tremor sources by combining multiple VTs and show that they are determined with location errors of approximately 1 km or less.

Moreover, with pushing their time resolution, the discussed method could bring insight on the complexity of the eruption dynamics as shown in Figures 7,8,9. For example, we observe in Figures 5 and 7b that for the January tremor, the spectral width is very low at the beginning and becomes larger and larger over time until it reaches a value equivalent to that corresponding to seismic noise. Conversely, for the October eruption we see in Figure 8b a more complicated temporal evolution for the spectral width that could reveal a more complex dynamic. By comparing with Figures 8a and 8c, we observe two main changes occurring at the same time from days 19.10.2010 and 27.10.2010, that are linked with intensification of the tremor amplitude visible on the seismograms. Thus such methods can also be useful to monitor the tremor intensity.

In a future, the methods presented here could be implemented at the OVPF. This would be particularly interesting in the case of the seismicity migration toward the eruptive site shown in Figure 14. Indeed, if the covariance matrix spectral width is computed in real-time in combination with an automatic 3D location based on the method described in this study, the position of the eruptive fracture could possibly be inferred more than one hour before the start of the eruption itself.

Another interesting prospective is to use the results of the multi-component analysis as input for algorithms of machine learning (ML), to build advanced approaches for detection and classification of different seismo-volcanic signals to be used in monitoring the activity and eruptive behavior of volcanoes. Figures 5 and 6 show that, in the space of parameters determined with the multi-component methods, different types of seismo-volcanic activity are separated and form relatively well defined clusters. It suggests that ML could be applied with this kind of "features" determined from the data of the PdF seismic network. Previous applications of machine learning to the PdF seismological data used features derived from individual sensors to study volcanic earthquakes (Hibert et al., 2017; Maggi et al., 2017) and tremors (Ren et al., 2019). The eventual advantage of multi-station features is that they incorporate inter-locations phase differences and are, therefore, sensitive to the location and the mechanism of the signal sources.

Acknowledgments

This study was financially supported by the European Research Council (ERC) under the European Union Horizon 2020 Research and Innovation Programme (grant agreement 787399-SEISMAZE) and by the Russian Ministry of Education and Science (grant N 14.W03.31.0033) for NS. Computations were performed using the IPGP High-Performance Computing infrastructure S-CAPAD (supported by the Ile-de-France region via the SEASAME programme, by France-Grille, and by the CNRS MASTODONS programme). The data used are publicly available and can be found online. The seismic data used for this study were provided by the Observatoire Volcanologique du Piton de la Fournaise (OVPF). The permanent network data (https://www.fdsn.org/networks/detail/PF/) can be downloaded from the IPGP Data Center (http://ws.ipgp.fr/fdsnws/dataselect/1/), the RESIF data center (http://ws.resif.fr/fdsnws/dataselect/1/), or the IRIS Data Management Center (IRIS-DMC, http://service.iris.edu/fdsnws/dataselect/1/). The UnderVolc data (https://doi.org/10.15778/RESIF.YA2009) are available from the RESIF data center.

References

Bachèlery, P. (1981). *Le Piton de la Fournaise (Ile de la Réunion): Etude volcanologique, structurale et pétrologique* (Thèse de doctorat).

Ballmer, S., Wolfe, C. J., Okubo, P. G., Haney, M. M., & Thurber, C. H. (2013). Ambient seismic noise interferometry in Hawai'i reveals long-range observability of volcanic tremor. *Geophysical Journal International*.

Battaglia, J., & Aki, K. (2003). Location of seismic events and eruptive fissures on the Piton de la Fournaise volcano using seismic amplitudes. *Journal of Geophysical Research*, *108*(B8).

Battaglia, J., Aki, K., & Ferrazzini, V. (2005b). Location of tremor sources and estimation of lava output using tremor source amplitude on the Piton de la Fournaise volcano : 1. Location of tremor sources. *Journal of Volcanology and Geothermal Research*, *147*, 268–290.

Battaglia, J., Brenguier, F., & Roult, G. (2016). Seismic Monitoring at Piton de la Fournaise. In P. Bachèlery, J.-F. Lénat, A. Di Muro, & L. Michon (Eds.), *Active Volcanoes of the South-west Indian Ocean* (pp. 223–242).

Bensen, G., Ritzwoller, M., Barmin, M., Levshin, A., Lin, F., Moschetti, M., ... Yang, Y. (2007). Processing seismic ambient noise data to obtain reliable broad-band

surface wave dispersion measurements. *Geophysical Journal International*, *169*(3), 1239–1260.

Bonneville, A. (1990). Structure de la lithosphre. In L. J.-F. (Ed.), *Le volcanisme de la réunion, monographie* (pp. 1–18).

Brenguier, F. (2014). *Undervolc experiment, 2009-2011, code ya (understanding volcanic processes). resif - rseau sismologique et godsique franais. terrestrial seismic network.* doi: 10.15778/RESIF.YA2009

Brenguier, F., Kowalski, P., Staudacher, T., Ferrazzini, V., Lauret, F., Boissier, P., ... Di Muro, A. (2012). First Results from the UnderVolc High Resolution Seismic and GPS Network Deployed on Piton de la Fournaise Volcano. *Seismological Research Letters*, *83*.

Chouet, B., & Matoza, R. (2013). A multi-decadal view of seismic methods for detecting precursors of magma movement and eruption. *Journal of Volcanology and Geothermal Research*, *252*, 108–175. Retrieved from `https://doi.org/10.1016/j.jvolgeores.2012.11.013`

Chouet, B. A. (1996, 03 28). Long-period volcano seismicity: its source and use in eruption forecasting. *Nature*, *380*, 309-316. Retrieved from `http://dx.doi.org/10.1038/380309a0` doi: 10.1038/380309a0

Courtillot, V., Besse, J., Vandamme, D., Montigny, R., Jaeger, J., & Cappetta, H. (1986). Deccan flood basalts at the Cretaceous/Tertiary boundary? *Earth and Planetary Science Letters*, *80*, 361–374. Retrieved from `https://doi.org/10.1016/0012-821X(86)90118-4`

De Barros, L., Bean, C., Zecevic, M., Brenguier, F., & Peltier, A. (2013). Eruptive fracture location forecasts from highfrequency events on Piton de la Fournaise Volcano. *Geophysical Research Letters*, *40*, 4599–4603.

Droznin, D., Shapiro, N., Droznina, S. Y., Senyukov, S., Chebrov, V., & Gordeev, E. (2015). Detecting and locating volcanic tremors on the Klyuchevskoy group of volcanoes (Kamchatka) based on correlations of continuous seismic records. *Geophysical Journal International*, *203*(2), 1001–1010.

Duputel, Z., Lengline, O., & Ferrazzini, V. (2019, January). Constraining Spatiotemporal Characteristics of Magma Migration at Piton De La Fournaise Volcano From Pre-eruptive Seismicity. *Geophysical Research Letters*, *46*(1), 119-127. Retrieved from `https://hal.archives-ouvertes.fr/hal-02108480` doi: 10.1029/2018GL080895

Endo, E. T., & Murray, T. (1991, Sep 01). Real-time seismic amplitude measurement (rsam): a volcano monitoring and prediction tool. *Bulletin of Volcanology*, *53*(7), 533–545. doi: 10.1007/BF00298154

Goldstein, P., & Chouet, B. (1994). Array measurements and modeling of sources of shallow volcanic tremor at Kilauea volcano, Hawaii. *Journal of Geophysical Research: Solid Earth*, *99*(B2), 2637–2652.

Haney, M. M. (2014). Backprojection of volcanic tremor. *Geophysical Research Letters*, *41*(6), 1923-1928. Retrieved from `https://agupubs.onlinelibrary.wiley.com/doi/abs/10.1002/2013GL058836` doi: 10.1002/2013GL058836

Hibert, C., Provost, F., Malet, J.-P., Maggi, A., Stumpf, A., & Ferrazzini, V. (2017). Automatic identification of rockfalls and volcano-tectonic earthquakes at the piton de la fournaise volcano using a random forest algorithm. *Journal of Volcanology and Geothermal Research*, *340*, 130 - 142. doi: https://doi.org/10.1016/j.jvolgeores.2017.04.015

Lénat, J.-F., & Bachèlery, P. (1990). Structure et fonctionnement de la zone centrale du Piton de la Fournaise. In J.-F. Lénat (Ed.), *Le volcanisme de La Réunion* (pp. 257–296).

Maggi, A., Ferrazzini, V., Hibert, C., Beauducel, F., Boissier, P., & Amemoutou, A. (2017, 03). Implementation of a Multistation Approach for Automated Event Classification at Piton de la Fournaise Volcano. *Seismological Research Letters*, *88*(3), 878-891. doi: 10.1785/0220160189

McNutt, S. R., & Nishimura, T. (2008). Volcanic tremor during eruptions: Temporal characteristics, scaling and constraints on conduit size and processes. *Journal of Volcanology and Geothermal Research*, *178*(1), 10 - 18. Retrieved from `http://www.sciencedirect.com/science/article/pii/S0377027308000991` (Dynamics of Volcanic Explosions: Field Observations, Experimental Constraints and Integrated Modelling of Volcanic Explosions: Field Observations, Experimental Constraints and Integrated Modelling) doi: https://doi.org/10.1016/j.jvolgeores.2008.03.010

McNutt, S. R., & Roman, D. C. (2015). Chapter 59 - volcanic seismicity. In H. Sigurdsson (Ed.), *The encyclopedia of volcanoes (second edition)* (Second Edition ed., p. 1011 - 1034). Amsterdam: Academic Press. Retrieved from `http://www.sciencedirect.com/science/article/pii/B9780123859389000596` doi: https://doi.org/10.1016/B978-0-12-385938-9.00059-6

Métaxian, J.-P., Lesage, P., & Valette, B. (2002). Locating sources of volcanic tremor and emergent events by seismic triangulation: Application to Arenal volcano, Costa Rica. *Journal of Geophysical Research: Solid Earth*, *107*(B10).

Mordret, A., Rivet, D., Lands, M., & Shapiro, N. M. (2015). Three-dimensional shear velocity anisotropic model of piton de la fournaise volcano (la runion island) from ambient seismic noise. *Journal of Geophysical Research: Solid Earth*, *120*(1), 406-427. doi: 10.1002/2014JB011654

OVPF. (2011). *Activity bulletin 08/01/2011, ISSN 2610-5101.*

Peltier, A., Famin, V., Bachlery, P., Cayol, V., Fukushima, Y., & Staudacher, T. (2008). Cyclic magma storages and transfers at Piton de La Fournaise volcano (la Réunion hotspot) inferred from deformation and geochemical data. *Earth Planet. Sci. Lett.*, *270*, 180–188. doi: 10.1016/j.epsl.2008.02.042

Permana, T., Nishimura, T., Nakahara, H., Fujita, E., & Ueda, H. (2019, 11). Reliability evaluation of volcanic tremor source location determination using cross-correlation functions. *Geophysical Journal International*, *220*(2), 1300-1315. Retrieved from `https://doi.org/10.1093/gji/ggz523` doi: 10.1093/gji/ggz523

Ren, C. X., Peltier, A., Ferrazzini, V., Rouet-Leduc, B., Johnson, P. A., & Brenguier, F. (2019). *Machine learning reveals the seismic signature of eruptive behavior at piton de la fournaise volcano.*

Roman, D. C., & Cashman, K. V. (2006, 06). The origin of volcano-tectonic earthquake swarms. *Geology*, *34*(6), 457-460. Retrieved from `https://doi.org/10.1130/G22269.1` doi: 10.1130/G22269.1

Roult, G., Peltier, A., Taisne, B., Staudacher, T., Ferrazzini, V., & Di Muro, A. (2012). A new comprehensive classification of the Piton de la Fournaise activity spanning the 1985-2010 period. Search and analysis of short-term precursors from a broad-band seismological station. *J. Volcanol. Geotherm. Res.*, *241*, 78–104.

Schmid, A. (2011). *Quelle prédictibilité pour les éruptions volcaniques ? de l'échelle mondiale au piton de la fournaise* (Thèse de doctorat).

Seydoux, L., de Rosny, J., & Shapiro, N. M. (2017, 06). Pre-processing ambient noise cross-correlations with equalizing the covariance matrix eigenspectrum. *Geophysical Journal International*, *210*(3), 1432-1449. doi: 10.1093/gji/ggx250

Seydoux, L., Shapiro, N., De Rosny, J., Brenguier, F., & Landes, M. (2016). Detecting seismic activity with a covariance matrix analysis of data recorded on seismic arrays.

Geophysical Journal International, *204*(3), 1430–1442.

Seydoux, L., Shapiro, N. M., de Rosny, J., & Landes, M. (2016). Spatial coherence of the seismic wavefield continuously recorded by the usarray. *Geophysical Research Letters*, *43*(18), 9644-9652. doi: 10.1002/2016GL070320

Shapiro, N., & Campillo, M. (2004). Emergence of broadband rayleigh waves from correlations of the ambient seismic noise. *Geophysical Research Letters*, *31*(7).

Shapiro, N. M., Campillo, M., Stehly, L., & Ritzwoller, M. H. (2005). High-resolution surface-wave tomography from ambient seismic noise. *Science*, *307*(5715), 1615–1618. doi: 10.1126/science.1108339

Shapiro, N. M., Ritzwoller, M. H., & Bensen, G. D. (2006). Source location of the 26 sec microseism from cross-correlations of ambient seismic noise. *Geophysical Research Letters*, *33*(18), L18310. doi: 10.1029/2006GL027010

Soubestre, J., Seydoux, L., Shapiro, N. M., de Rosny, J., Droznin, D. V., Droznina, S. Y., ... Gordeev, E. I. (2019). Depth migration of seismovolcanic tremor sources below the klyuchevskoy volcanic group (kamchatka) determined from a network-based analysis. *Geophysical Research Letters*, *46*(14), 8018-8030. doi: 10.1029/2019GL083465

Soubestre, J., Shapiro, N. M., Seydoux, L., deRosny, J., Droznin, D. V., Droznina, S. Y., ... Gordeev, E. I. (2018). Network-based detection and classification of seismovolcanic tremors: Example from the klyuchevskoy volcanic group in kamchatka. *Journal of Geophysical Research: Solid Earth*, *123*(1), 564-582. doi: 10.1002/2017JB014726

Staudacher, T., Peltier, A., Ferrazzini, V., Di Muro, A., Boissier, P., Catherine, P., ... Lebreton, J. (2016). Fifteen Years of Intense Eruptive Activity (1998-2013) at Piton de la Fournaise volcano: a Review. In P. Bachèlery, J.-F. Lénat, A. Di Muro, & L. Michon (Eds.), *Active Volcanoes of the South-west Indian Ocean* (pp. 139–170). doi: 10.1007/978-3-642-31395-0_9

Taisne, B., Brenguier, F., Shapiro, N. M., & Ferrazzini, V. (2011, feb). Imaging the dynamics of magma propagation using radiated seismic intensity. *Geophys. Res. Lett.*, *38*(4), 2–6. doi: 10.1029/2010GL046068

Tsekhmistrenko, M., Sigloch, K., & Hosseini, K. (2018, Apr). Whole-mantle structure under the Reunion hotspot in the western Indian Ocean from multifrequency P-wave tomography. In *EGU General Assembly Conference Abstracts* (p. 1076).

Unglert, K., & Jellinek, A. M. (2015). Volcanic tremor and frequency gliding during dike intrusions at klaueaa tale of three eruptions. *Journal of Geophysical Research: Solid*

Earth, *120*(2), 1142-1158. doi: 10.1002/2014JB011596

Unglert, K., Radi, V., & Jellinek, A. (2016). Principal component analysis vs. self-organizing maps combined with hierarchical clustering for pattern recognition in volcano seismic spectra. *Journal of Volcanology and Geothermal Research*, *320*, 58 - 74. doi: https://doi.org/10.1016/j.jvolgeores.2016.04.014